JOURNAL OF PROPULSION AND POWER
Vol. 39, No. 4, July–August 2023

Flame Dynamics in the Combustion Chamber of Hybrid Rocket Using Multiangle Chemiluminescence

Jiaxiao Luo,* Zelin Zhang,† Xin Lin,‡ Zezhong Wang,§ Wu Kun,¶ Gongxi Zhou,* Senhao Zhang,* Fei Li,** and Xilong Yu**
State Key Laboratory of High Temperature Gas Dynamics, Chinese Academy of Science, 100190 Beijing, People's Republic of China
and
Jie Wu††
Science and Technology on Optical Radiation Laboratory, 100845 Beijing, People's Republic of China

https://doi.org/10.2514/1.B38955

The flame dynamics in the combustion chamber of a hybrid rocket motor were visualized using novel chemiluminescence imaging. A multidirectional visualization system employing 3×1 endoscopes generated images based on methylidyne chemiluminescence (CH*), with one endoscope in the precombustion chamber and two in the postcombustion chamber. Images were collected with a high-speed camera using a 1 ms exposure and a 1 kHz frame rate. Fuel grains having a helical or a conventional circular port structures were assessed, and combustion trials were conducted using a laboratory-scale hybrid rocket motor with oxygen as the oxidizer at mass flow rates from 10.43 to 18.51 g/s: equivalent to combustion chamber pressures ranging from 0.7 to 1.24 MPa. Flame structures were observed during the ignition, combustion, and shutdown stages; and the helical grain generated a larger, more intense flame zone. A proper orthogonal decomposition analysis showed that the helical grains also produced a greater degree of turbulence and stronger oscillations. These results confirm that a helical structure increases the flow turbulence and convective heat transfer in the combustion chamber. These effects lead to higher regression rates and better mixing efficiency that may, in turn, provide greater combustion efficiency at optimized oxidizer/fuel ratios.

I. Introduction

HYBRID rocket motors typically use liquid oxidizer together with solid fuel as the propellant system and provide the advantages of high reliability, a good margin of safety, and low cost as compared with conventional liquid or solid propulsion systems. As a result of these features, hybrid rocket motors are highly attractive with regard to many applications, such as sounding rockets, suborbital systems, and commercial aerospace vehicles [1]. However, the diffusive turbulent flames in these motors lead to low fuel grain regression rates, which have hindered the further development of hybrid rockets [2]. Various research has attempted to mitigate this limitation via approaches including the use of multiport geometries [3], fuel additives [4–6], and paraffin-based fuel grains [7,8].

Modulating the flowfield inside the combustion chamber by employing complex grain port geometries is a useful means of improving the regression rate [9–19], especially with the rapid development of additive manufacturing (AM). AM enables the simple yet rapid production of grains with complicated geometries that would be infeasible for traditional manufacturing methods. As an example, Whitmore et al. [15] greatly improved the regression rate of acrylonitrile–butadiene–styrene (ABS) fuel grains by manufacturing grains with a helical port structure using AM. In addition, Bisin et al. [11] embedded pure paraffin in a gyroid cellular structure fabricated by three-dimensional printing, and thus increased the regression rates by 15 to 35% as compared with pure paraffin. Wang et al. [16,17] embedded paraffin-based fuels in ABS substrates having helical structures, leading to a 20% increase in the regression rate.

Although the aforementioned studies all improved the regression rate, the role of a complex port geometry in the combustion process is still not understood. Some numerical studies [20,21] have indicated that a helical structure increases the intensity of flow turbulence inside the combustion chamber to enhance heat transfer, but experimental verification of this phenomenon has not yet been provided. Thus, it would be helpful to develop an effective in situ diagnostic method to improve our understanding of flame dynamics.

In recent years, various optically based, nonintrusive flame imaging methods have been applied to the study of flame dynamics, including planar laser-induced fluorescence (PLIF), tomographic laser absorption spectroscopy (TAS), Rayleigh scattering (RS), and chemiluminescence imaging. PLIF is a non-path-integral technique and features high sensitivity, high spatial resolution, and species specificity. It uses a selected narrow spectral width planar laser sheet to excite the chemical species of interest (such as electronically excited hydroxyl (OH*) radical) in the flowfield. The target chemical species then gets excited from a specific rotational–vibrational level in its ground state to a rotational–vibrational level in the excited electronic state. Next, it undergoes a spontaneous transition back to the ground electronic state, and the fluorescence is emitted. The emitted fluorescence signals then get detected by a camera to indicate the flame frontier. Nevertheless, the field of view is often limited, and quantitative interpretation of the

Received 4 July 2022; revision received 10 November 2022; accepted for publication 10 January 2023; published online 23 February 2023.

*Ph.D. Candidate, Institute of Mechanics; also School of Engineering Science, University of Chinese Academy of Sciences, 100049 Beijing, People's Republic of China.

†Master's Student, Institute of Mechanics; also College of Mechatronics Engineering, North University of China, Taiyuan 030051, People's Republic of China.

‡Senior Engineer, Institute of Mechanics; also University of Chinese Academy of Sciences, 100049 Beijing, People's Republic of China; linxin_bit@imech.ac.cn (Corresponding Author).

§Postdoctoral Student, Institute of Mechanics; also School of Engineering Science, University of Chinese Academy of Sciences, 100049 Beijing, People's Republic of China; wangzezhong@imech.ac.cn (Co-Corresponding Author).

¶Associate Professor, Institute of Mechanics; also School of Engineering Science, University of Chinese Academy of Sciences, 100049 Beijing, People's Republic of China.

**Professor, Institute of Mechanics; also School of Engineering Science, University of Chinese Academy of Sciences, 100049 Beijing, People's Republic of China.

††Senior Engineer.

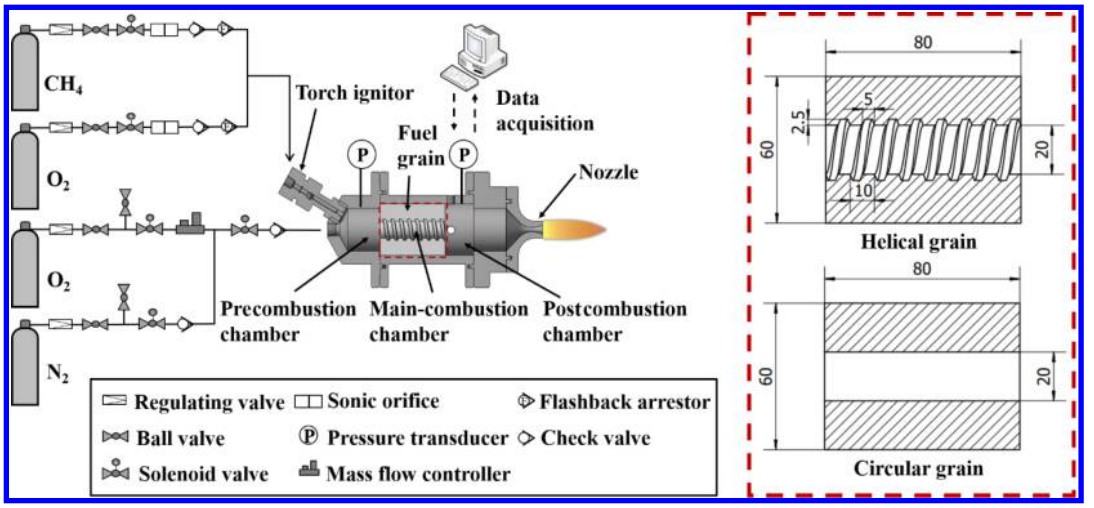

Fig. 1 Diagram of the laboratory-scale hybrid rocket motor system and the fuel grain configuration.

signal requires independent information concerning local quenching rates, which greatly limit the applications in turbulent flames [22]. RS is another well-established technique for the measurement of temperature, but its signal depends on local gas composition, which is generally unknown in reactive flows [23]. TAS can effectively quantify the time-resolved temperature and partial pressure of a target gas species during combustion [24–27]. However, the tradeoff between spatial resolution and the complex experimental design associated with this technique makes it very difficult to apply to real-world propulsion systems. In contrast, chemiluminescence imaging is a promising means of addressing practical issues related to analyzing flame dynamic. Chemiluminescence is the emission of light when the molecule in an unstable excited state produced by the reaction decay to the more stable ground state. This nonintrusive path-integral measurement method provides a qualitative indication of heat release rates, local equivalence ratios, and excited radical concentrations without the use of laser equipment [28]. Additionally, it can be easily coupled with optical fibers, significantly simplifying the experimental equipment. By virtue of these advantages, chemiluminescence imaging has been used to diagnose the combustion characteristics of numerous propulsion systems, such as gas turbines [29–32], scramjets [33–35], and pulse detonation engines [36,37].

Chemiluminescence imaging has also been used to visualize the combustion processes in hybrid rocket motors. Jens et al. [38] employed OH* chemiluminescence imaging to observe the combustion flame generated by a slab burner using both classical and paraffin fuels at elevated pressures. The droplet entrainment of the paraffin fuel grain was studied, and the position and thickness of the flame zone inside the boundary layer were identified based on the resulting images. Similarly, Petrarolo et al. [39] investigated Kelvin–Helmholtz instability during the combustion of liquefying hybrid rocket fuels by applying OH* chemiluminescence imaging to a slab paraffin burner. Using the images generated by this technique, the flame topology and location were determined. Although these works provide information concerning hybrid rocket combustion mechanisms, it should be noted that the slab burner's chamber pressure and chamber temperature may be much lower than that of the actual motor. Additionally, the flame of a slab burner is one-dimensional, which is the axial dimension. The flame structure on the radial and tangential directions is unobservable. Choi et al. [40] visualized the flame in the postcombustion chamber of a hybrid rocket using methylidyne chemiluminescence (CH*) imaging as a means to study the low-frequency instability. However, because the quartz window through which images were acquired was contaminated soon after ignition, the flame could only be observed in the initial stage of the combustion process; and the images could not be used for the analysis of the flame dynamics in the main combustion chamber. Yuasa et al. [41] visualized the flame in the main combustion chamber of a hybrid rocket motor via a large quartz window positioned in the precombustion chamber. Even so, this prior work primarily focused on the swirl structure of the flame and did not examine dynamical behavior. It should also be noted that the imaging method used in such studies can greatly affect the structure of the motor, such as the designs of the swirl injector and ignitor.

In this work, the flame in the main-combustion chamber of a hybrid rocket motor was visualized and studied using a novel chemiluminescence imaging technique. Specifically, multidirectional internal visualization of the flame in the combustion chamber was performed based on a custom-made 3×1 bundled optical fiber. One fiber was placed in the precombustion chamber with its main optical axis positioned at an angle of 30 deg relative to the axis of symmetry of the fuel grain, whereas the remaining two fibers were situated in the postcombustion chamber with their main optical axes perpendicular to the axis of symmetry. A helical grain was selected for use in the firing tests, and a conventional circular fuel grain was used for comparison. The firing tests were conducted at oxygen mass flux values from 14.43 to 18.51 g/s and at combustion chamber pressures from 0.71 to 1.24 MPa. Raw images of the two grains were compared and analyzed in detail, whereas a proper orthogonal decomposition (POD) analysis was used to assess the flame oscillation behavior. Finally, the effect of a helical structure on the flame dynamics was established based on the regression rates and characteristic velocities.

II. Experimental Setup and Methodology

A. Laboratory-Scale Hybrid Rocket Motor and Fuel Grain

A diagram of the laboratory-scale hybrid rocket motor used in this work is provided in Fig. 1. Further information regarding the apparatus can be found in previous publications [16–18]. The motor used gaseous oxygen as the oxidizer and a CH_4/O_2 torch ignitor activated by a spark plug to ignite the fuel grain. The oxidizer injector and the ignitor were both installed in the precombustion chamber of the motor. The oxygen mass flow rate was controlled by a mass flow controller (Bronkhost model F-203AV) with an accuracy of $\pm(0.5\% + 0.1\%$ FS (full scale)). Nitrogen was used to purge the combustion chamber after each trial. Two pressure transducers sampling at a frequency of 1 kHz were positioned in the pre- and postcombustion chambers of the motor. The timing sequence of each firing test is presented in Table 1.

Table 1 Timing sequence of the firing tests

Serial number	Time, s	Action
1	0.0	Data acquisition turned on
2	10.0	Oxygen supply turned on
3	17.0	Ignitor turned on
4	18.0	Ignitor turned off
5	20.0	Oxygen turned off/nitrogen turned on
6	25.0	Data acquisition turned off

Polyethylene fuel grains having helical or circular geometries as shown in Fig. 1 were employed. A helical grain was selected because this shape is known to improve the regression rate and is considered to be a typical kind of complex grain shape [21,42]. The helical grain was 80 mm in length, 20 mm in the inner diameter, and 60 mm in the outer diameter. The thread pitch was 10 mm, the groove width was 5 mm, and the groove height was 3 mm. As noted, a conventional circular fuel grain was used for comparison, with an inner diameter of 20 mm and an outer diameter and length that were the same as those of the helical grain.

Four groups of tests were conducted, and each group comprised one helical grain firing and one circular grain firing at approximately the same oxygen mass flow rate. It should be noted that some variations in the oxygen mass flow rate unavoidably occurred as a consequence of changes in experimental parameters, including the different combustion chamber pressures and valve response times. The average oxygen mass flow rate during these trials ranged from 10.43 to 18.51 g/s, corresponding to a mass flux of oxygen from 3.32 to 6.21 g/(cm^{2}s). The test conditions are summarized in Table 2.

B. Optical Setup

The CH* chemiluminescence imaging system is shown in Fig. 2. A specially customized 3×1 bundled optical fiber was used in the imaging system, and gradient-index (GRIN) lenses were employed to direct the optical images to the fiber inputs. Each lens had field-of-view angles of 50 deg and a diameter of 2 mm. A specially designed sapphire protection kit with a diameter of 5 mm was used to protect each lens from the high-temperature gas in the combustion chamber. One lens was placed in the precombustion chamber with its optical axis positioned at an angle of 30 deg relative to grain. This allowed the majority of the combustion chamber to be observed while not affecting the oxygen injection process. Using this lens, three sections of the fuel grain's front face could be monitored, as shown in Fig. 2. Here, the region labeled point I corresponds to the front face of the grain, whereas point II was located between the front and end edges of the fuel grain. This was the area within the main-combustion chamber in which the mixture of oxygen and pyrolyzed fuel reacted and was the main region of interest in the present work. Point III indicates the flame zone in the postcombustion chamber. The other two lenses were placed in the postcombustion chamber, with the main optical axis of each perpendicular to the fuel grain's axis of symmetry (designated as section II-II in Fig. 2). These two view angles allowed the end edge of the fuel grain and the flame in the postcombustion chamber to be clearly observed. The bundled fibers were then connected to a fast-speed camera (Photron SA-Z). The frame rate and exposure time for the camera were 1 kHz and 1 ms, respectively. A center wavelength of 430 nm, a bandwidth of 10 nm, and a narrowband filter were used to image the CH* radicals.

Table 2 Firing test conditions

Group	Type of grain	Average mass flow rate of O_2 g/s	Average mass flux of O_2, g/(cm^{2}s)
1	Helical	17.83	5.48
	Circular	18.51	6.21
2	Helical	15.22	4.84
	Circular	14.70	4.68
3	Helical	11.89	3.67
	Circular	12.26	3.90
4	Helical	10.64	3.38
	Circular	10.43	3.32

C. Proper Orthogonal Decomposition Analysis

POD analysis is matrix factorization method. This process was used to convert the original image series into a set of linearly uncorrelated variables referred to as a mode to classify the dominant patter of the flame and to provide a good characterization of the flame dynamics and related time series of the imaging [43]. POD assumes that the continuously changing series of flame images can be linearly superimposed using multiple orthogonal modes according to the equation

$$\phi(x,t) = \phi_0 + \sum_{i=1}^{M} \alpha_i(t)\phi_i(x) \tag{1}$$

where x is a spatial coordinate (in units of pixels), t is the time sequence, α_i is the time coefficient of the temporal mode, ϕ_i is the spatial distribution characteristic of the mode, ϕ_0 is the mean value of the image series, and M is the total number of modes.

In this analysis, an image containing W pixels in each row and L pixels in each column forms a pixel matrix of $m = L \times W$. The image series can then be expressed as an $m \times n$ data matrix A, where n is the total number of images. After the mean value of each row of A is subtracted from A, this matrix can be decomposed into the product of three matrices via singular value decomposition [44] to find the orthogonal modes as

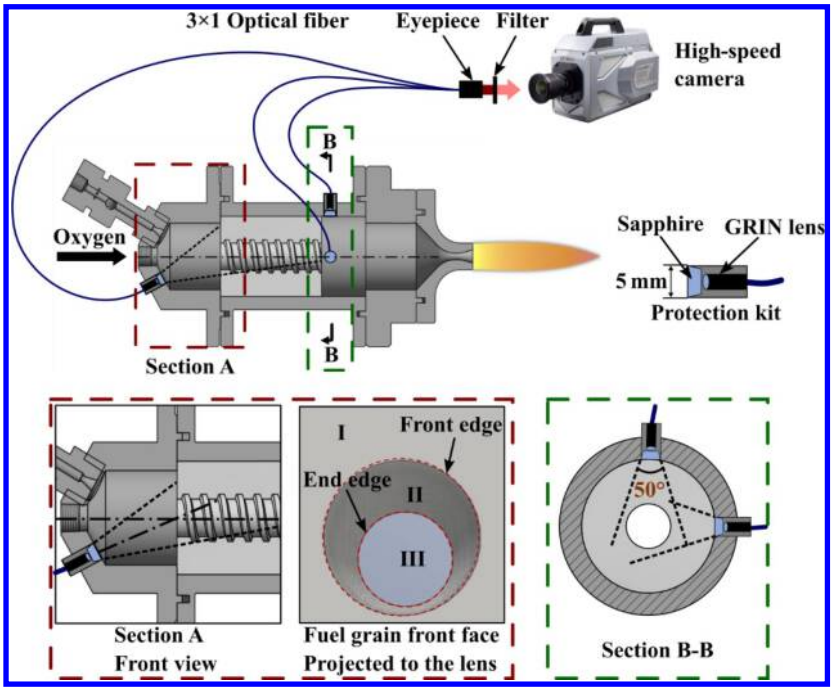

Fig. 2 Diagram of the imaging system.

$$A_{m\times n} = U_{m\times m} S_{m\times n} V^T_{n\times n} \tag{2}$$

Here, T is the transpose of a matrix; and U, S, and V represent the orthogonal modes of the flame series and their corresponding mode energy and time coefficients. To solve the three matrices of U, S, and V, a snapshot method [43,45] was used to simplify Eq. (2) as follows:

$$A^T A = V S^2 V^T \tag{3}$$

Equation (3) was then multiplied on the right by V, and we substitute $S = \sqrt{\lambda}$ to obtain

$$A^T A V = V S^2 = V\lambda \tag{4}$$

V and S can be obtained by solving the eigenvalue problem of $A^T A$. Then, U can be obtained by $US = AV$. The ith column of matrix U is the spatial distribution of mode i. The ith column of matrix V multiplied by the ith value of matrix S gives the time coefficient α_i of mode i. If the eigenvalues λ were sorted in a descending order, the energy at the start of the sequence would be dominant in the flame dynamic behavior. Subsequently, the normalized energy proportion of each mode$i$ can be calculated by Eq (5):

$$E_i = \frac{\lambda_i}{\sum_{j=0}^{M} \lambda_j} \tag{5}$$

III. Results and Discussion

A. Pressure and CH* Intensity Variations

Figure 3 plots the CH* intensity for both the precombustion and postcombustion chambers along with the combustion chamber pressure variation of firing test group 3. The CH* intensity used here is the mean pixel value of the raw image, and the CH* intensity in the postcombustion chamber is calculated by averaging the CH* intensities of the two lenses. In the case of both helical and circular grains, the CH* intensity in the postcombustion chamber decreases soon after the pressure in the combustion chamber increases. This phenomenon is primarily attributed to the carbon soot produced by incomplete combustion. A similar experiment phenomenon was previously reported in Ref. [40]. In contrast, the trend exhibited by the CH* intensity in the precombustion chamber matches that of the pressure.

It is apparent that the average chamber pressure and average CH* intensity produced by the helical grain were both higher than those generated during the circular trial. The chemiluminescence oscillations of the helical grain were more intense than those of the circular grain. This effect likely occurred because the helical structure increased the turbulence intensity of the flow in the chamber. As a result, the mixing of the fuel and oxidizer is more sufficient, leading to a more intense combustion.

B. Raw Image Analysis

Figures 4 and 5 present the flame images obtained during the combustion of the helical and circular grains, respectively, at times 1 and 2, as specified in Fig. 3. At time 1, all three lenses were able to provide clear images of the flames in both the main-combustion and postcombustion chambers (top row of Fig. 4). Additionally, the three sections specified in Fig. 2 can be clearly identified in Fig. 4a. However, as the combustion proceeded, the lenses in the postcombustion chamber were quickly contaminated and observations were no longer possible, whereas the lens in the precombustion chamber remained clear (Fig. 4d). This trend was consistent with the CH* intensity variations seen in Fig. 3.

The images of the helical grain in Figs. 4b and 4c indicate that the flame in the postcombustion chamber did not fill the entire field of view and that the intensity distribution was quite uneven. One possible reason for this observation is that the flame was not fully developed during the startup stage.

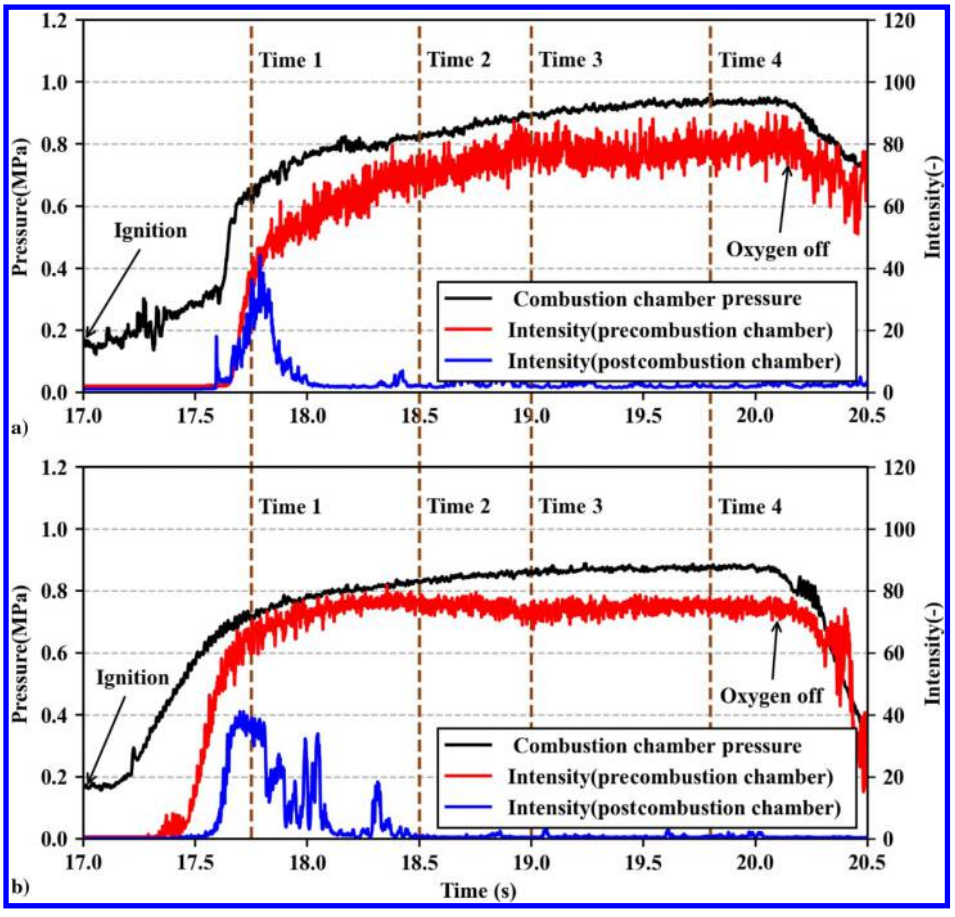

Fig. 3 CH* intensity and pressure variations over time during combustion of a) a helical grain and b) a circular grain.

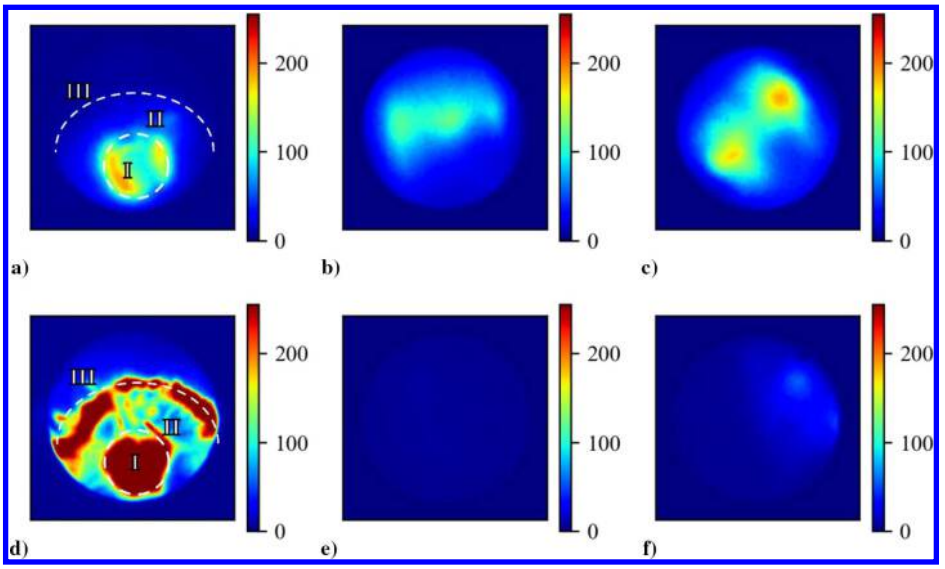

Fig. 4 Chemiluminescence images of the helical grain at time 1 (top row) and time 2 (bottom row), showing the flame in the main-combustion chamber (Figs. 4a and 4d), and the postcombustion chamber (Figs. 4b, 4c, 4e, and 4f).

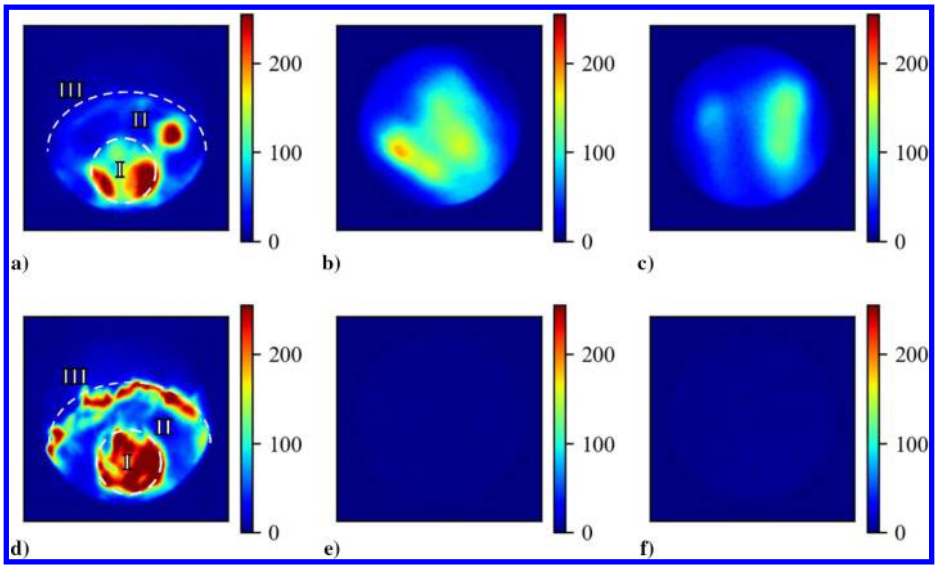

Fig. 5 Chemiluminescence images of the circular grain at time 1 (top row) and time 2 (bottom row), showing the flame in the main-combustion chamber (Figs. 5a and 5d), and the postcombustion chamber (Figs. 5b, 5c, 5e, and 5f) .

The data obtained from the circular grain exhibit similar features, although the flame zones at time 2 in the precombustion chamber are smaller than that generated in the helical grain trial. This difference can be ascribed to the increased flow turbulence and wider flame zone obtained with the helical grain.

C. Characteristics of the Chemiluminescence Image Obtained from the Precombustion Chamber

Figures 6 and 7 show series of instantaneous images together with time averages of these images acquired over specific durations in trials with the helical and circular fuel grains following four time points. The time interval for each frame is 5 ms, and the averages are generated for a time span of 40 ms.

From Fig. 6, it is evident that the dynamic behavior of the flame generated by the helical grain can be described by several stages. At time 1, when the pressure in the combustion chamber began to increase, the flame was primarily located in the postcombustion chamber with very little in the main-combustion chamber. As the combustion proceeded at time 2, the flame in the main-combustion chamber was established in the boundary layer close to the surface of the fuel grain. The flame in the postcombustion chamber also continued to develop such that it occupied almost all the chamber, and the chemiluminescence intensity increased rapidly. In the next phase at time 3, the thickness of the flame zone in the main-combustion chamber increased significantly, possibly as the mixing of the oxidizer and pyrolyzed fuel was promoted and the gaseous reaction layer in the combustion chamber increased in size. Filamentlike structures also appeared in the main-combustion chamber, likely as a result of the turbulence flow induced by the helical grain. However, at time 4, there was a decrease in both the flame intensity and the flame zone thickness in the main-combustion chamber. These effects can possibly be explained by the gradual erosion of the helical structure as combustion proceeded such that turbulence in the main-combustion chamber was reduced.

Similar stages are apparent in the images obtained in the trial using the circular grain, as presented in Fig. 7. However, there were three differences in the flame dynamics of the two fuel grains. First, the flame generated by the helical fuel grain exhibited more intense turbulent fluctuations and oscillations. This phenomenon was possibly a result of the increased flow turbulence generated by the helical structure in the main-combustion chamber. In the time-averaged figures, the intensity of the flame produced by the helical grain in the main-combustion

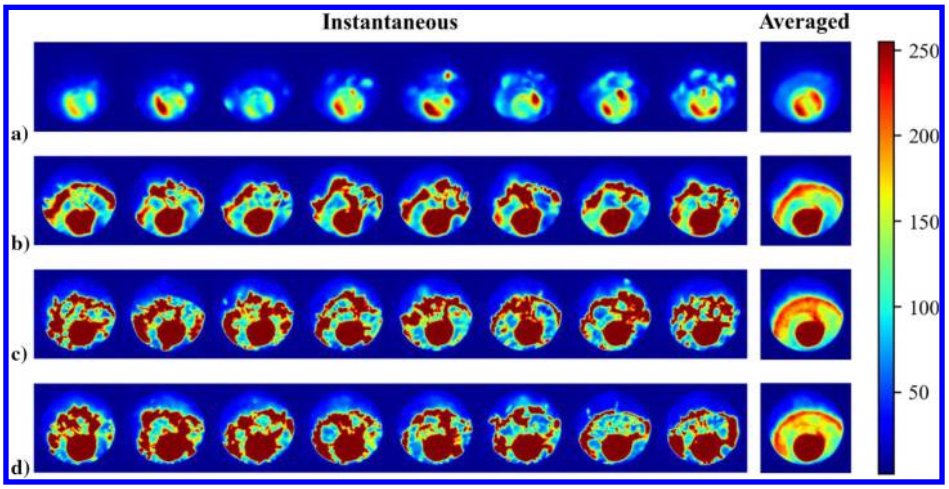

Fig. 6 Instantaneous and averaged images of the flame in the main-combustion chamber of the helical grain over short time spans beginning at a) time 1, b) time 2, c) time 3, and d) time 4.

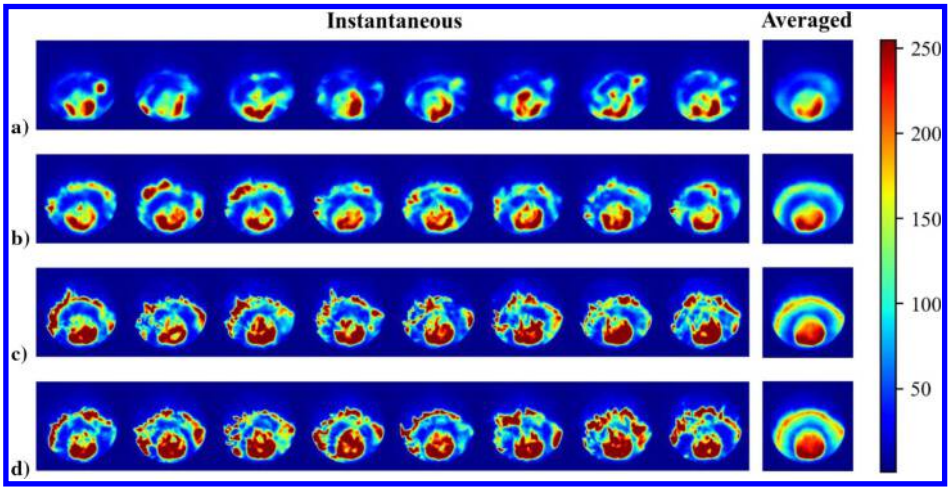

Fig. 7 Instantaneous and averaged images of the flame in the main-combustion chamber of the circular grain over short time spans beginning at a) time 1, b) time 2, c) time 3, and d) time 4.

chamber is higher and the flame zone is thicker. These findings suggest that the increased flow turbulence induced by the helical grain promoted the mixing of the oxidizer and the pyrolyzed fuel gas, resulting in a thicker flame region and increased gaseous reaction layer in the combustion chamber. Furthermore, there was no decrease in the flame zone thickness in the trial with the circular grain, likely because there was no change in the port geometry throughout the combustion process. Thus, the averaged flame structure remained stable.

D. POD Analysis of the Flame Structure

To further understand the flame dynamics inside the combustion chamber, a POD analysis was used to investigate the oscillation behavior of the flames. The first six modes of both the helical and circular grains are shown in Fig. 8. Each mode represents the overlying fluctuation, with the red and blue areas indicating regions with significant variations in the gas phase reactions. It is evident that detailed information concerning the flame dynamics in the boundary layer within the combustion chamber was obtained for both grains. In contrast, the flame oscillations in the postcombustion chamber were relatively unclear, possibly as a result of its full development. In the cases of almost all modes, the helical grain generated more intense variations that were also distributed over wider areas. The number of layers of intense variation regions produced by the helical grain were also higher. Because the intense variation regions indicate the regions where significant variations of the reaction intensity take place, the more intense the variation regions in the POD mode, the more

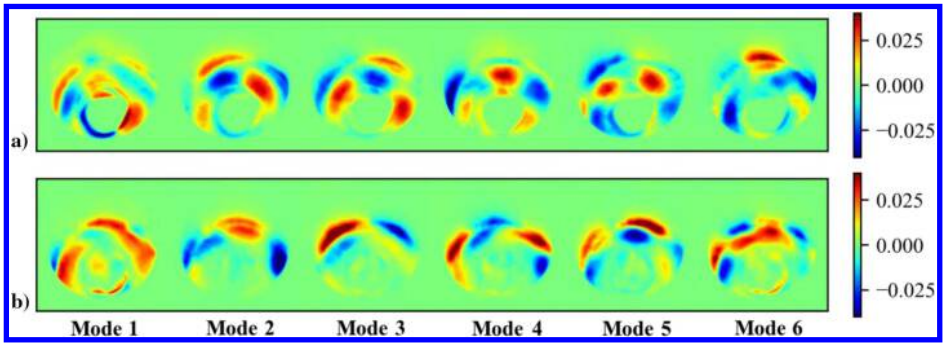

Fig. 8 The first six modes of the a) helical grain and b) circular grain.

oscillating the flame is likely to be. These results suggest that, in the case of the helical grain, the flame fluctuations were much stronger, possibly because of the stronger flow turbulence caused by the helical structure. This finding is in agreement with the raw image analysis. In the images of the postcombustion chamber, there were flame fluctuations for the circular case but none for the helical. The primary reason is that the flame of the helical grain in the postcombustion chamber was fully developed; as a result, no intense variation of reaction intensity was observed. This suggests the helical structure can enhance the mixing of the reactants to produce more complete combustion in the postcombustion chamber.

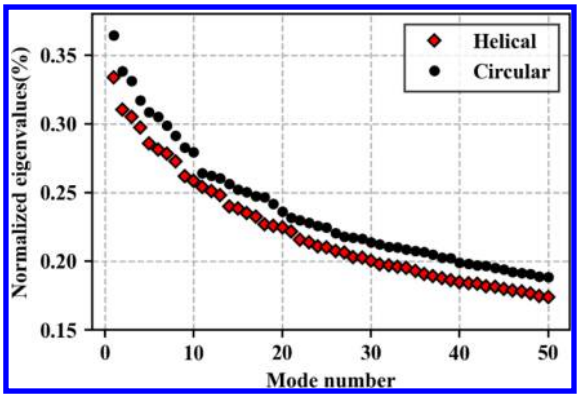

Fig. 9 Mode energy distributions for both grains.

The energy proportion of each mode indicates its relative importance of the corresponding mode, and so this parameter is important. Figure 9 plots the normalized energy values of the first 50 modes and demonstrates that the first mode counted for more than 0.3% of the total energy. In both cases, the energy proportion decreased significantly with the increase in the mode number, especially over the first 10 modes. Interestingly, the normalized eigenvalues of the first 50 modes for the helical grain were all smaller than those for the circular grain. Because lower modes often contain fewer oscillations, this finding suggests a more intense turbulent combustion occurred in the helical grain, which is also in agreement with the previous analysis of the raw images.

Figure 10 shows the variations of the time coefficients of the first four modes for both the helical and circular grains. It can be seen that the time coefficients of the first mode fluctuated around the value of zero, and the value is less than 0.1 for both the helical and circular grains. This result shows that the combustion process in the combustion chamber was relatively stable and that there was no obvious thermoacoustic coupling instability. Although the time coefficients of the other first four modes all showed oscillations around zero, they can be regarded as weights assigned to the first mode.

A fast Fourier transform was applied to the time coefficients of the oscillation modes of the flame to determine whether a dominant oscillation frequency was presented, with the results shown in Fig. 11. Note that for the sake of simplicity, only the first three modes are examined here. These frequency–amplitude plots confirm that the time coefficients for the first three modes of both grains had no obvious dominant frequency except for a minor spike at approximately 18 Hz in

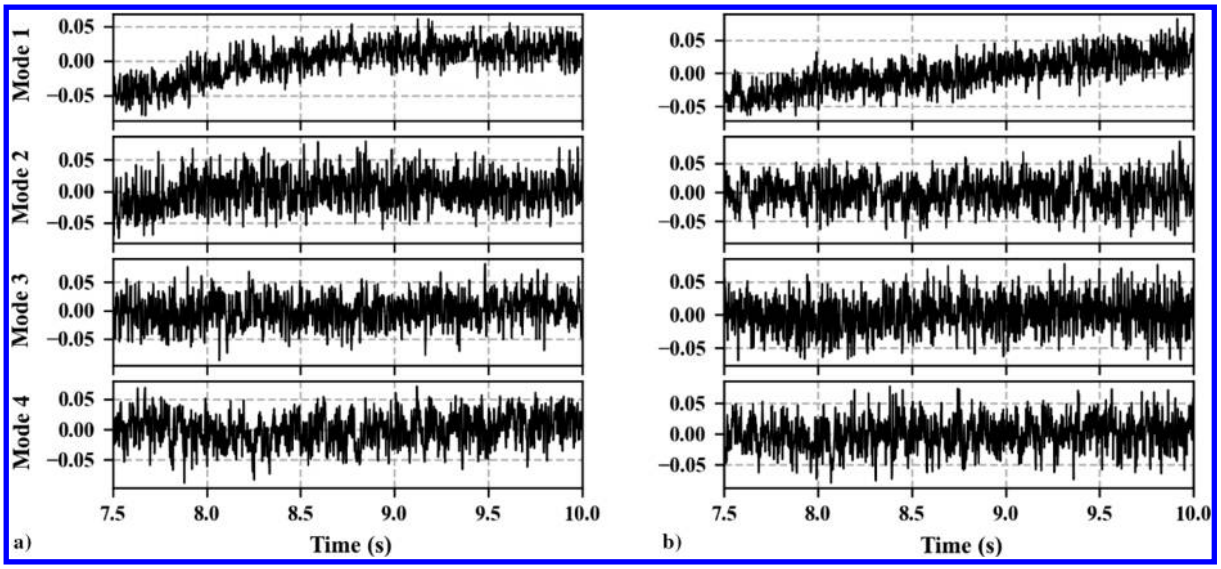

Fig. 10 Time coefficient variations during the combustion of the a) helical and b) circular grains.

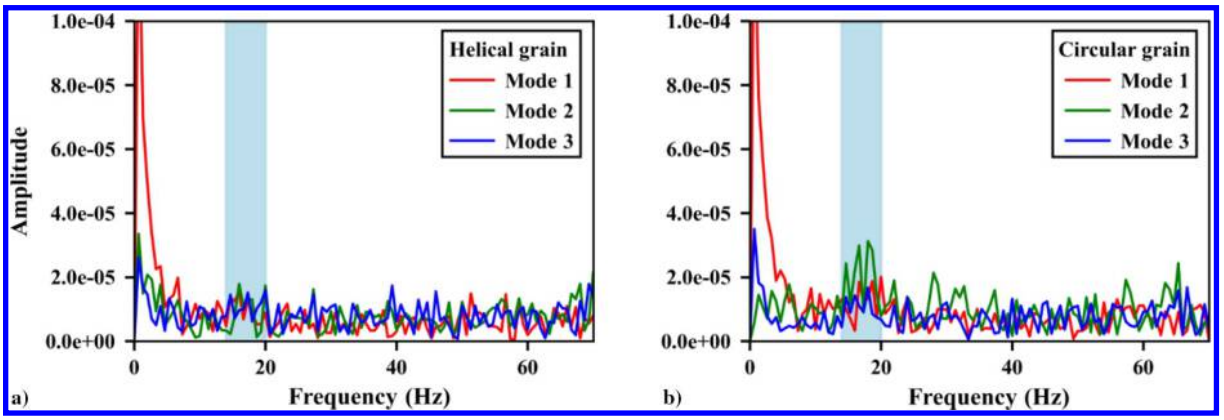

Fig. 11 Frequency–amplitude plots of the time coefficients of the a) helical and b) circular grains.

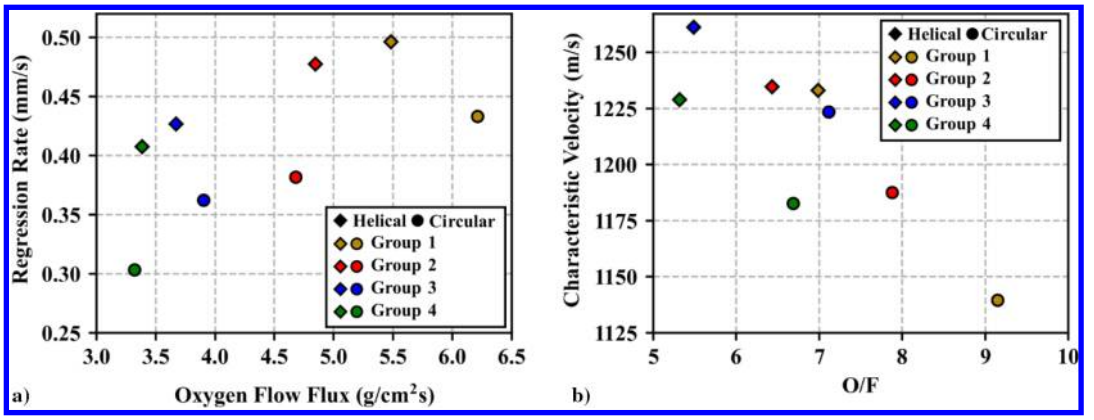

Fig. 12 Comparison of the a) regression rates and b) characteristic velocity of the helical and circular grains.

the case of the circular grain. Therefore, there was no obvious thermoacoustic coupling instability caused by the helical structure in the combustion chamber. In fact, the helical fuel grains may even have suppressed the combustion instability. Although similar instability is not found in the pressure and CH* intensity variations, it may be related to lens contamination during the firing test and the combustion chamber configurations of this paper. The reasons for this anomalous phenomenon are not fully understood, and more systematic studies including theoretic work will be necessary.

E. Regression Rate and Characteristic Velocity

The regression rate and the combustion characteristic velocity are the two most important parameters for a hybrid rocket motor because they are closely related to the specific impulse, thrust, and combustion efficiency. Thus, these two parameters were analyzed in the present work to further assess the effects of the helical structure on the flame dynamics in the combustion chamber.

The fuel grain regression rate refers to the speed at which the fuel surface burns back, and it can be calculated as

$$\dot{r}_{\text{ave}} = \frac{d_f - d_0}{2t} \tag{6}$$

where d_0 and d_f are the average inner diameter of the initial fuel grain and the fuel grain after the firing test, respectively. In the case of a helical fuel grain, the latter term is modified to account for the uneven port geometry to

$$d_f = \sqrt{d_0^2 + \frac{4(m_{f0} - m_f)}{\pi \rho L}} \tag{7}$$

Here, m_{f0} and m_f are the masses of the fuel grain before and after the firing test, whereas L is the length and ρ is the average density of the fuel grain.

The characteristic velocity is another important parameter related to combustion performance. A higher characteristic velocity at a fixed oxidizer/fuel ratio means better combustion efficiency. The characteristic velocity is usually defined as

$$C^* = \frac{A_t}{M_t} P_c \tag{8}$$

where A_t is the nozzle throat area, M_t is the mass of the fuel and oxidizer consumed, and P_c is the combustion chamber pressure.

Figure 12 plots the regression rates and the characteristic velocity of each fuel grain as function of the oxidizer mass flow fluxes and oxidizer/fuel ratio, respectively. As shown in Fig. 12a, for both the helical and circular grains, the regression rate increased along with the oxidizer flow flux and the regression rate of the helical grain was always higher than that of the circular grain by roughly 20%. Because the heat needed for the pyrolysis of the solid fuel grain is mostly determined by convective heat transfer, as indicated by the classical hybrid rocket combustion theory [1,46], this increased regression rate confirms that there is a higher convective heat transfer in the helical grain. This further proves that the helical structure can effectively increase the flow turbulence in the combustion chamber, which is in agreement with the aforementioned analysis of the flame dynamics. In addition, the characteristic velocity of the helical grain was uniformly higher (Fig. 12b). Although the characteristic velocities are not compared at the same oxygen/fuel (O/F) ratios here (because of the different regression rates of the motors), it can be expected that the combustion efficiency of a helical grain will be higher than that of a circular grain under more suitable experimental conditions.

IV. Conclusions

The dynamic behaviors of the flames in the combustion chamber of a hybrid rocket motor were successfully characterized and analyzed in this work using multiangle endoscopic CH* chemiluminescence imaging. Firing experiments were conducted on a laboratory-scale hybrid rocket motor using oxygen as the oxidizer at mass flow rates ranging from 10.43 to 18.51 g/s, corresponding to combustion chamber pressures from 0.7 to 1.24 MPa. Raw image analysis showed that the flame generated by the helical grain in the combustion chamber exhibited stronger fluctuations and a thicker flame zone as compared with the circular grain. These effects are attributed to the greater flow turbulence in the combustion chamber in the former case. A POD analysis showed that, for each mode of the flame in the combustion chamber, the helical grain generated more layers of intense gas phase reaction zones. This result indicates that the fluctuation characteristics of the helical grain were stronger than those of the circular grain. Additionally, spectrum analysis of the time coefficients suggested that the helical grain suppressed the combustion instability. The regression rates of the helical grain were approximately 20% higher than those obtained using the circular grains, presumably because the greater turbulence in the former enhanced heat transfer in the combustion chamber. The characteristic velocity provided by the helical grain was also higher. Although the oxidizer/fuel ratio differed greatly between the two grains, at optimized ratios, a helical grain is expected to provide higher combustion efficiency than a circular grain.

Acknowledgments

This study was financed in part by the National Natural Science Foundation of China (grant nos. 92271117, 11802315, 11927803, 11872368, and 12072355), the Key-Area Research and Development Program of Guangdong Province (grant no. 2021B0909060004), and the Youth Innovation Promotion Association of the Chinese Academy of Sciences (grant no. 2022018).

References

[1] Kuo, K. K., and Chiaverini, M. J., *Fundamentals of Hybrid Rocket Combustion and Propulsion*, AIAA, Reston, VA, 2007, pp. 32–33. https://doi.org/10.2514/4.866876

[2] Kobald, M., Schmierer, C., Ciezki, H., Schlechtriem, S., Toson, E., and De Luca, L., "Viscosity and Regression Rate of Liquefying Hybrid Rocket Fuels," *Journal of Propulsion and Power*, Vol. 33, No. 5, 2017, pp. 1245–1251. https://doi.org/10.2514/1.B36207. 10.2514/1.B36207

[3] Ahn, B., Kang, H., Lee, E., Yun, Y., and Kwon, S., "Design of Multiport Grain with Hydrogen Peroxide Hybrid Rocket," *Journal of Propulsion and Power*, Vol. 34, No. 5, 2018, pp. 1189–1197. https://doi.org/10.2514/1.B36949

[4] Carmicino, C., and Russo Sorge, A., "Experimental Investigation into the Effect of Solid-Fuel Additives on Hybrid Rocket Performance," *Journal of Propulsion and Power*, Vol. 31, No. 2, 2015, pp. 699–713. https://doi.org/10.2514/1.B35383

[5] Hashim, S. A., Karmakar, S., and Roy, A., "Effects of Ti and Mg Particles on Combustion Characteristics of Boron–HTPB-Based Solid Fuels for Hybrid Gas Generator in Ducted Rocket Applications," *Acta Astronautica*, Vol. 160, July 2019, pp. 125–137. https://doi.org/10.1016/j.actaastro.2019.04.002

[6] Sun, X., Tian, H., Yu, N., and Cai, G., "Regression Rate and Combustion Performance Investigation of Aluminum Metallized HTPB/98HP Hybrid Rocket Motor with Numerical Simulation," *Aerospace Science and Technology*, Vol. 42, April–May 2015, pp. 287–296. https://doi.org/10.1016/j.ast.2015.01.014

[7] Karabeyoglu, A., Zilliac, G., Cantwell, B. J., DeZilwa, S., and Castellucci, P., "Scale-Up Tests of High Regression Rate Paraffin-Based Hybrid Rocket Fuels," *Journal of Propulsion and Power*, Vol. 20, No. 6, 2004, pp. 1037–1045. https://doi.org/10.2514/1.3340

[8] Zilliac, G., Waxman, B. S., Karabeyoglu, A. M., Cantwell, B., and Evans, B. J., "Peregrine Hybrid Rocket Motor Development," AIAA Paper 2014-3870, 2014. https://doi.org/10.2514/6.2014-3870

[9] Oztan, C., and Coverstone, V., "Utilization of Additive Manufacturing in Hybrid Rocket Technology: A Review," *Acta Astronautica*, Vol. 180, March 2021, pp. 130–140. https://doi.org/10.1016/j.actaastro.2020.11.024

[10] Oztan, C., Ginzburg, E., Akin, M., Zhou, Y., Leblanc, R. M., and Coverstone, V., "3D Printed ABS/Paraffin Hybrid Rocket Fuels with Carbon Dots for Superior Combustion Performance," *Combustion and Flame*, Vol. 225, March 2021, pp. 428–434. https://doi.org/10.1016/j.combustflame.2020.11.024

[11] Bisin, R., Paravan, C., Alberti, S., and Galfetti, L., "A New Strategy for the Reinforcement of Paraffin-Based Fuels Based on Cellular Structures: The Armored Grain—Mechanical Characterization," *Acta Astronautica*, Vol. 176, Nov. 2020, pp. 494–509. https://doi.org/10.1016/j.actaastro.2020.07.003

[12] Zilliac, G., Story, G. T., Karp, A. C., Jens, E. T., and Whittinghill, G., "Combustion Efficiency in Single Port Hybrid Rocket Engines," AIAA Paper 2020-3746, 2020. https://doi.org/10.2514/6.2020-3746

[13] Young, G., Connell, T. L. Jr, Fennell, K., Possehl, S., and Baier, M., "Examining Port Geometry/Solid Loading for Additively Manufactured Fuels in Hybrid Rockets," *Journal of Propulsion and Power*, Vol. 37, No. 2, 2021, pp. 305–313. https://doi.org/10.2514/1.B38033

[14] Joshi, S. C., and Sheikh, A. A., "3D Printing in Aerospace and Its Long-Term Sustainability," *Virtual and Physical Prototyping*, Vol. 10, No. 4, 2015, pp. 175–185. https://doi.org/10.1080/17452759.2015.1111519

[15] Whitmore, S. A., Walker, S. D., Merkley, D. P., and Sobbi, M., "High Regression Rate Hybrid Rocket Fuel Grains with Helical Port Structures," *Journal of Propulsion and Power*, Vol. 31, No. 6, 2015, pp. 1727–1738. https://doi.org/10.2514/1.B35615

[16] Wang, Z., Lin, X., Li, F., and Yu, X., "Combustion Performance of a Novel Hybrid Rocket Fuel Grain with a Nested Helical Structure," *Aerospace Science and Technology*, Vol. 97, Feb. 2020, Paper 105613. https://doi.org/10.1016/j.ast.2019.105613

[17] Wang, Z., Lin, X., Li, F., Zhang, Z., and Yu, X., "Improving the Combustion Performance of a Hybrid Rocket Engine Using a Novel Fuel Grain with a Nested Helical Structure," *Journal of Visualized Experiments*, Vol. 167, Jan. 2021, Paper e61555. https://doi.org/10.3791/61555

[18] Lin, X., Qu, D., Chen, X., Wang, Z., Luo, J., Meng, D., Liu, G., Zhang, K., Li, F., and Yu, X., "Three-Dimensional Printed Metal-Nested Composite Fuel Grains with Superior Mechanical and Combustion Properties," *Virtual and Physical Prototyping*, Vol. 17, No. 3, 2022, pp. 437–450. https://doi.org/10.1080/17452759.2022.2035934

[19] Quadros, F. D., and Lacava, P. T., "Swirl Injection of Gaseous Oxygen in a Lab-Scale Paraffin Hybrid Rocket Motor," *Journal of Propulsion and Power*, Vol. 35, No. 5, 2019, pp. 896–905. https://doi.org/10.2514/1.B37283

[20] Tian, H., Yu, R., Zhu, H., Wu, J., and Cai, G., "Three-Dimensional Numerical and Experimental Studies on Transient Ignition of Hybrid Rocket Motor," *Acta Astronautica*, Vol. 140, Nov. 2017, pp. 247–254. https://doi.org/10.1016/j.actaastro.2017.08.022

[21] Tian, H., Li, Y., Li, C., and Sun, X., "Regression Rate Characteristics of Hybrid Rocket Motor with Helical Grain," *Aerospace Science and Technology*, Vol. 68, Sept. 2017, pp. 90–103. https://doi.org/10.1016/j.ast.2017.05.006

[22] Ma, L., Li, X., Sanders, S. T., Caswell, A. W., Roy, S., Plemmons, D. H., and Gord, J. R., "50-KHz-Rate 2D Imaging of Temperature and H_2O Concentration at the Exhaust Plane of a J85 Engine Using Hyperspectral Tomography," *Optics Express*, Vol. 21, No. 1, 2013, pp. 1152–1162. https://doi.org/10.1364/OE.21.001152

[23] Li, S., Farooq, A., and Hanson, R. K., "H2O Temperature Sensor for Low-Pressure Flames Using Tunable Diode Laser Absorption near 2.9 μm," *Measurement Science and Technology*, Vol. 22, No. 12, 2011, Paper 125301. https://doi.org/10.1088/0957-0233/22/12/125301

[24] Cai, T., Wang, G., Cao, Z., Zhang, W., and Gao, X., "Sensor for Headspace Pressure and H_2O Concentration Measurements in Closed Vials by Tunable Diode Laser Absorption Spectroscopy," *Optics and Lasers in Engineering*, Vol. 58, July 2014, pp. 48–53. https://doi.org/10.1016/j.optlaseng.2013.12.005

[25] Guo, X., Zheng, F., Li, C., Yang, X., Li, N., Liu, S., Wei, J., Qiu, X., and He, Q., "A Portable Sensor for In-Situ Measurement of Ammonia Based on near-Infrared Laser Absorption Spectroscopy," *Optics and Lasers in Engineering*, Vol. 115, April 2019, pp. 243–248. https://doi.org/10.1016/j.optlaseng.2018.12.005

[26] Zhang, G., Wang, G., Huang, Y., Wang, Y., and Liu, X., "Reconstruction and Simulation of Temperature and CO2 Concentration in an Axisymmetric Flame Based on TDLAS," *Optik*, Vol. 170, Oct. 2018, pp. 166–177. https://doi.org/10.1016/j.ijleo.2018.05.123

[27] Wang, Z., Deguchi, Y., Kamimoto, T., Tainaka, K., and Tanno, K., "Pulverized Coal Combustion Application of Laser-Based Temperature Sensing System Using Computed Tomography–Tunable Diode Laser Absorption Spectroscopy (CT-TDLAS)," *Fuel*, Vol. 268, May 2020, Paper 117370. https://doi.org/10.1016/j.fuel.2020.117370

[28] Wang, K., Li, F., Zeng, H., and Yu, X., "Three-Dimensional Flame Measurements with Large Field Angle," *Optics Express*, Vol. 25, No. 18, 2017, pp. 21,008–21,018. https://doi.org/10.1364/OE.25.021008

[29] Hardalupas, Y., Panoutsos, C., and Taylor, A., "Spatial Resolution of a Chemiluminescence Sensor for Local Heat-Release Rate and Equivalence Ratio Measurements in a Model Gas Turbine Combustor," *Experiments in Fluids*, Vol. 49, No. 4, 2010, pp. 883–909. https://doi.org/10.1007/s00348-010-0915-z

[30] Ruan, C., Chen, F., Cai, W., Qian, Y., Yu, L., and Lu, X., "Principles of Non-Intrusive Diagnostic Techniques and Their Applications for Fundamental Studies of Combustion Instabilities in Gas Turbine Combustors: A Brief Review," *Aerospace Science and Technology*, Vol. 84, Jan. 2019, pp. 585–603. https://doi.org/10.1016/j.ast.2018.10.002

[31] Arndt, C. M., Severin, M., Dem, C., Stöhr, M., Steinberg, A. M., and Meier, W., "Experimental Analysis of Thermo-Acoustic Instabilities in a Generic Gas Turbine Combustor by Phase-Correlated PIV, Chemiluminescence, and Laser Raman Scattering Measurements," *Experiments in Fluids*, Vol. 56, No. 4, 2015, pp. 1–23. https://doi.org/10.1007/s00348-015-1929-3

[32] Guethe, F., Guyot, D., Singla, G., Noiray, N., and Schuermans, B., "Chemiluminescence as Diagnostic Tool in the Development of Gas Turbines," *Applied Physics B*, Vol. 107, No. 3, 2012, pp. 619–636. https://doi.org/10.1007/s00340-012-4984-y

[33] Miller, J. D., Peltier, S. J., Slipchenko, M. N., Mance, J. G., Ombrello, T. M., Gord, J. R., and Carter, C. D., "Investigation of Transient Ignition Processes in a Model Scramjet Pilot Cavity Using Simultaneous 100 kHz Formaldehyde Planar Laser-Induced Fluorescence and CH* Chemiluminescence Imaging," *Proceedings of the Combustion Institute*, Vol. 36, No. 2, 2017, pp. 2865–2872. https://doi.org/10.1016/j.proci.2016.07.060

[34] Kato, N., and Im, S., "Flame Dynamics Under Various Backpressures in a Model Scramjet with and Without a Cavity Flameholder," *Proceedings of the Combustion Institute*, Vol. 38, No. 3, 2021, pp. 3861–3868. https://doi.org/10.1016/j.proci.2020.07.110

[35] Nakaya, S., Yamana, H., and Tsue, M., "Experimental Investigation of Ethylene/Air Combustion Instability in a Model Scramjet Combustor Using Image-Based Methods," *Proceedings of the Combustion Institute*, Vol. 38, No. 3, 2021, pp. 3869–3880. https://doi.org/10.1016/j.proci.2020.07.129

[36] Cuppoletti, D., Ombrello, T., Carter, C., Hammack, S., and Lefkowitz, J., "Ignition Dynamics of a Pulse Detonation Igniter in a Supersonic Cavity Flameholder," *Combustion and Flame*, Vol. 215, May 2020, pp. 376–388. https://doi.org/10.1016/j.combustflame.2020.01.030

[37] Ombrello, T. M., Carter, C. D., Tam, C.-J., and Hsu, K.-Y., "Cavity Ignition in Supersonic Flow by Spark Discharge and Pulse Detonation," *Proceedings of the Combustion Institute*, Vol. 35, No. 2, 2015, pp. 2101–2108. https://doi.org/10.1016/j.proci.2014.07.068

[38] Jens, E. T., Karp, A. C., Miller, V. A., Hubbard, G. S., and Cantwell, B. J., "Experimental Visualization of Hybrid Combustion: Results at Elevated Pressures," *Journal of Propulsion and Power*, Vol. 36, No. 1, 2020, pp. 33–46. https://doi.org/10.2514/1.B37416

[39] Petrarolo, A., Kobald, M., and Schlechtriem, S., "Understanding Kelvin–Helmholtz Instability in Paraffin-Based Hybrid Rocket Fuels," *Experiments in Fluids*, Vol. 59, No. 4, 2018, Paper 62. https://doi.org/10.1007/s00348-018-2516-1

[40] Choi, G., Moon, Y. J., and Lee, C., "Visualization of Flow Dynamics in the Post Chamber of Hybrid Rocket Using Chemiluminescence Images," AIAA Paper 2015-3827, 2015. https://doi.org/10.2514/6.2015-3827

[41] Yuasa, S., Ide, T., Masugi, M., Sakurai, T., Shiraishi, N., and Shimada, T., "Visualization and Emission Spectra of Flames in Combustion Chamber of Swirling-Oxidizer-Flow-Type Hybrid Rocket Engines," *Journal of Thermal Science and Technology*, Vol. 6, No. 2, 2011, pp. 268–277. https://doi.org/10.1299/jtst.6.268

[42] Lee, C., Na, Y., and Lee, G., "The Enhancement of Regression Rate of Hybrid Rocket Fuel by Helical Grain Configuration and Swirl Flow," AIAA Paper 2015-3827, 2005. https://doi.org/10.2514/6.2005-3906

[43] Taira, K., Brunton, S. L., Dawson, S. T. M., Rowley, C. W., Colonius, T., McKeon, B. J., Schmidt, O. T., Gordeyev, S., Theofilis, V., and Ukeiley, L. S., "Modal Analysis of Fluid Flows: An Overview," *AIAA Journal*, Vol. 55, No. 12, 2017, pp. 4013–4041. https://doi.org/10.2514/1.J056060.

[44] Strang, G., Strang, G., Strang, G., and Strang, G., *Introduction to Linear Algebra*, Wellesley-Cambridge Press, Wellesley, MA, 1993, pp. 382–385.

[45] Allery, C., Béghein, C., and Hamdouni, A., "Applying Proper Orthogonal Decomposition to the Computation of Particle Dispersion in a Two-Dimensional Ventilated Cavity," *Communications in Nonlinear Science and Numerical Simulation*, Vol. 10, No. 8, 2005, pp. 907–920. https://doi.org/10.1016/j.cnsns.2004.05.005

[46] Marxman, G. A., Muzzy, R., and Wooldridge, C., "Fundamentals of Hybrid Boundary Layer Combustion," *Heterogeneous Combustion Conference*, AIAA Paper 1963-0505, 1963. https://doi.org/10.2514/6.1963-505

E. L. Petersen
Associate Editor